Renzo Danilo (Orcid ID: 0000-0001-8139-6462)

Multiaxial fatigue behavior of additively manufactured Ti6Al4V alloy: axial-torsional proportional loads

Danilo A. Renzo[a], Emanuele Sgambitterra[a], Pietro Magarò[a], Franco Furgiuele[a], Carmine Maletta[a], Carlo Alberto Biffi[b], Jacopo Fiocchi[b], Ausonio Tuissi[b]

[a]DIMEG - Dept. of Mechanical, Energy and Management Engineering, University of Calabria, 87036, Rende, Italy
[b]CNR ICMATE, National Research Council - Institute of Condensed Matter Chemistry and Technologies for Energy, Unit of Lecco, Via Previati 1/e, 23900 Lecco, Italy

Acknowledgements

This work was supported by the regional program "POR Calabria FSE/FESR 2014-2010", within the context of "Smart Specialization Strategy - S3 Calabria (Italy)", topic: "Smart Manufacturing".

Abstract

Additive Manufacturing (AM) techniques are under constant development and Selective Laser Melting (SLM) is among the most promising ones. However, widespread use of AM techniques in many industries is limited by the different/unusual mechanical properties of AM metallic parts, with respect to traditionally processed ones, especially when dealing with complex fatigue loading conditions. In fact, crack formation and propagation mechanisms are mainly affected by the development of internal defects, residual stresses and microstructural changes. This is actually one of the major issues the materials engineering community is facing today. In many applications AM components are subjected to multiaxial fatigue loads, arising from operating conditions and/or from complex geometries, that unavoidably generate crack initiation and propagation mechanisms.

The aim of this study is to investigate the multiaxial fatigue behavior of additively manufactured Ti6Al4V samples, made by SLM. Fatigue tests, combining proportional axial and torsional loads, were performed on thin-walled tubular specimens. Full field measurement techniques, such as the infrared thermography (IR) and digital image correlation (DIC), were also used to capture temperature and strain evolutions, at both local and global scales. Fatigue results highlighted damage mechanisms and failure modes are strongly related to the applied stress level.

Keywords: Multiaxial fatigue; Select Laser Melting; Additive Manufacturing; Ti6Al4V; Infrared Thermographic technique; Digital Image Correlation.

1. Introduction

Titanium alloys, and in particular the Ti6Al4V compound, is widely used for high-demanding applications in many engineering fields, from aerospace and automotive to chemical and biomedical industries [1,2,3,4]. In fact, it exhibits good mechanical properties, remarkable corrosion resistance, and excellent biocompatibility [5,6]. The most conventional way to manufacture complex shaped Ti6Al4V components is based on casting, forging and rolling processes, usually followed by machining. However, additive manufacturing (AM) technologies are gaining increasing interest and attention from both technical and scientific communities. In fact, the development and application of AM technologies are rapidly increasing in the last years, because they allow to easily obtain components with complex and/or custom designs [4,7]. AM technology is defined by the American Society for Testing and Materials (ASTM), as the "processes of joining materials to make objects from three-dimensional (3D) model data, usually layer upon layer, as opposed to subtractive manufacturing methodologies" [8]. AM can be used to manufacture different materials, from metals to polymers, and they can be classified according to the energy source for material melting (e.g. electron beam, laser), feeding system (powder bed versus blown powder) and feed stock form (wire or powder) [9]. They include the Laser beam/Electron beam Powder Bed Fusion (L-PBF or E-PBF), the Directed Energy Deposition (DED) and the Selective Laser Melting (SLM) [10,11]. This latter process uses a high-power density laser to melt metallic powders layer by layer and it is increasingly used for several high-demanding engineering applications, especially when dealing high-performance and/or chemically active metals, such as the titanium-based alloys.

However, it is well known that AM processes usually affect the metallurgical and mechanical properties of additively manufactured components with respect to the wrought material. In particular, they inherently lead to the formation of internal porosity and defects/flaws, residual stresses and microstructural changes, depending on several process parameters/conditions. Unfortunately, all these features represent key factors for crack formation and propagation mechanisms and, consequently, they lead to reduced fatigue properties. Significant/critical process conditions include the printing strategy, e.g. interlayer distance and laser path, the substrate temperature and cooling rate, the laser parameters and the quality/size of the feed stock powder [12,13].

Within this scenario, different R&D activities have been undertaken in last years, with the aim of better understanding the fatigue behavior of Ti6Al4V AM components, with a particular focus on uniaxial loading conditions [14,15]. It was demonstrated that AM materials always exhibit a lower fatigue strength with respect to the wrought ones. In particular, a marked decrease of the fatigue strength, around 40–50%, was observed by Wycisk et al. and Fatemi et al. [16,17]. This was directly attributed to the high surface roughness, that acts as multiple stress concentrators, tensile residual stresses, subsurface pores and defects. All these features promote crack initiation and propagation, resulting in a reduced fatigue strength [18,19,20]. In addition, AM processes, could cause material anisotropies, depending on the building/deposition paths, that generate direction-dependent mechanical behavior [21]. It was shown that the tensile strength along the build direction is slightly lower than the in-plane ones. These anisotropies play a significant role on the fatigue response of AM parts [22], especially when dealing with multiaxial conditions. Therefore, the design of the building strategy represents a critical task as it significantly affects the mechanical properties of the final component. For this reason, different laser scanning strategies and heat treatments have been assessed with the aim of reducing the anisotropies and improving the mechanical proprieties of Ti6Al4V AM parts [23,24]. It was demonstrated that fatigue resistance of AM parts can be improved by post machining operations and/or by stress relieving processes [25]. Leuders et al. [26] demonstrated

that heat treatment at 1050°C for 2h under vacuum conditions could improve the fatigue strength by an order of magnitude. Similar results were obtained by Fatemi et al. [27] that performed torsional fatigue tests on Ti6Al4V AM heat-treated samples. They also demonstrated a significant improvement of the fatigue response of AM samples after post machining operations, as a direct consequence of the lower surface roughness and surface defect density. However, the improvement is limited by the presence of internal and near surface defects. Multiaxial fatigue properties of AM Ti6Al4V was also investigated by Fatemi et al. [17], through combined axial and torsional loads, under both proportional and non-proportional conditions. In fact, direct transferability of the uniaxial fatigue results, based on standard equivalent stress and/or strain criteria, cannot be carried out mainly due to the direction-dependent mechanical properties of AM parts. Systematic comparisons between AM and wrought samples were also made by Fatemi et al. [17]. As expected, it was found that internal and near-surface porosity/defects cause marked reductions in the fatigue properties of AM samples. In addition, brittle fracture always occurs, with the crack plane normal to the maximum tensile stress. On the contrary, shear cracking and ductile fracture mainly occurs in wrought specimens. Multiaxial fatigue tests of a titanium alloy was also carried out by Wu et al. [28], under both proportional and non-proportional axial-torsional loads. A multiaxial fatigue life prediction model was proposed based on the maximum shear strain amplitude and a modified Smith Watson and Topper parameter.

Even if these recent investigations provide useful insights about the multiaxial fatigue response of AM parts, further studies should be carried out for a deeper understanding of the key damage mechanisms as well as to develop effective and reliable predictive models.

Within this context, this study reports early results of a research project on the multiaxial fatigue response of AM Ti6Al4V samples, made by Selective Laser Melting (SLM). Multiaxial fatigue conditions were obtained by combining proportional axial-torsional loads. The main focus of the research consists in the analysis of damage evolution at both global and local scales, occurring during multiaxial fatigue loadings. To this aim, Infrared Thermography (IR) and Digital Image Correlation (DIC) techniques were used to capture full-field temperature and strain maps during the experiments. Results highlighted damage mechanisms and failure modes are strongly related to the applied stress level.

2. Material and methods

2.1. Materials and manufacturing process

Thin-walled tubular specimens with a wall thickness of 0.85 mm were designed based on the ASTM Standard E2207 - 15 [29] (see Fig. 1a). AM samples were made by SLM (AM400 Fro Renishaw), by using a spherical micrometric powder of Ti6Al4V (average size equal to 45 μm), whose main process parameters are listed in Table 1.

The laser scanning strategies used for SLM manufacturing is contour–meander type in order to reduce the anisotropy of the samples. The scanning pattern is rotated of 67° at each layer and the process is repeated every 180 layers during the growth of the sample (Fig. 1b).

As-built AM samples were heat-treated at 850 °C for 1 hour in vacuum followed by cooling in protective atmosphere. Specimens were subsequently machined and polished (diamond compound: 9 μm and 3 μm), at both the outer and inner surfaces, before testing. The final roughness measured at the outer surface was $R_a \approx 0.2$ μm.

Monotonic tensile and torsional tests, under displacement and rotation-controlled mode (1 mm/min and 3 deg/min), respectively, were performed to measure the static mechanical properties of AM samples. Figure 2 shows the engineering measured stress-strain curves

obtained from both tests and main mechanical parameters are reported in Tab. 2. Yield stresses, namely σ_Y and τ_Y, were measured by using the offset method at 0.2%. In addition, comparisons with the properties of AM samples by Fatemi at al. [17] and of wrought material are given in the Table.

2.2. Fatigue tests: method and equipment

Multiaxial fatigue experiments were carried by an electrodynamic testing machine (Instron, ElectroPulse E10000) with load capacities of 10 kN and 100 Nm. Tests were performed at room temperature by combined proportional axial-torsion loads (see Fig. 3), at a frequency of 10 Hz and with a run-out of $2 \cdot 10^6$ cycles. Special care was adopted to the specimen alignment and to avoid any spurious loads [31]. Preliminary tests were also carried out by full field DIC measurements to verify the alignment before each test. In-phase sinusoidal waveforms were adopted, as shown in Fig. 3, under stress control conditions with a stress ratio R=0.05 ($R = \sigma_{\min}/\sigma_{\max} = \tau_{\min}/\tau_{\max}$). The ratio between normal and shear stresses was kept constant ($\tau/\sigma = \sqrt{3}/3$) in all experiments, that provide the same nominal von Mises stresses for the two loads.

The applied stress levels, in terms of axial stress amplitude (σ_a), axial mean stress (σ_m), shear stress amplitude (τ_a) and shear mean stress (τ_m), are summarized in Table 3. The table also reports the maximum von Mises equivalent stress ($\sigma_{eq,max}$) together with the ratio with respect to the ultimate tensile stress ($\sigma_{eq,max}/\sigma_U$). Tests were carried out at increasing maximum equivalent stresses ranging from $\sigma_{eq,max}/\sigma_U = 0.2$ to 0.61.

In-situ full field measurements were carried out, by infrared thermography (IR) and digital image correlation (DIC), to capture global and local temperature and strain evolution during fatigue experiments. In particular, simultaneous IR and DIC measurements were made for each testing samples as illustrated in Fig. 4. For this purpose, one side of the specimen was black painted, to obtain a good surface emissivity (0.95) for IR investigations, whereas a speckle pattern with an appropriate grayscale distribution was applied on the other side to allow the correlation analysis.

IR images, with frame rate of 12.5 fps, were captured by using an infrared camera (FLIR, A615) having a resolution of 640x480 pixels and thermal sensitivity < 0.05°C. Results were analyzed by a commercial IR imaging software (FLIR, Tools+).

A digital camera (Sony ICX 625- Prosilica GT 2450 model) with a resolution of 2448 by 2050 pixels was used to capture DIC images with a frame rate of 15 fps. A Linos Photonics objective and a Rodagon lens (f. 80 mm) were used to get a proper magnification and to focus the entire gauge length of the samples. In these conditions, a scale of approximately 90 pixels/mm was obtained. In order to collect a significant number of images to provide an in-depth analysis into the fatigue cycles, loading frequency was periodically decreased at 0.25 Hz. Only 5 cycles were performed during this latter stage in order to prevent sudden drop of the temperature dictated by the decrease of the loading frequency.

Correlation analyses were carried out by a commercial software for 2D analysis (Vic-2D Correlated Solution), using a subset size of 51 pixels and a distance between the centers of the subsets of 5 pixels.

As 2D digital image correlation analysis does not directly provide the out of plane displacement component, namely u_x, generated by the multiaxial loads (see Fig. 5), they were calculated, as schematically depicted in Fig. 5, from the in plane measured displacements u_y:

$$u_x = u_y \tan\vartheta \tag{1}$$

where $\vartheta = \sin^{-1}(y/R_o)$, y is the generic distance from the axis of the sample and R_o is the outer radius. The accuracy of this method was verified by comparisons with 3D digital analyses and good agreements were observed as shown in Fig. 5. In fact, 3D analyses require a much complex experimental setup and higher computational costs. Displacements results were used to calculate the strain field experienced by the sample during the fatigue experiments. Figure 5 also shows a schematic depiction of virtual extensometers, a tool of the image correlation software, that is used to calculate the strain components.

3. Results and discussion

3.1 Fatigue life

Multiaxial fatigue results obtained from the experiments, in terms of both equivalent von Mises stress and strain amplitudes, as a function of the number of reversals to failure, are reported in Table 4. The corresponding fatigue resistance curves are shown in Figs. 6a-b. These figures also show typical failure modes of the samples, as discussed in the following section.

The von Mises equivalent strain was calculated, at the outer surface of the sample, according to the following equation [32,33]:

$$\varepsilon_{eq} = \frac{1}{(1+\nu_{el})\sqrt{2}}\sqrt{\left(\varepsilon_x - \varepsilon_y\right)^2 + \left(\varepsilon_y - \varepsilon_z\right)^2 + (\varepsilon_z - \varepsilon_x)^2 + 6\left[\left(\frac{\gamma_{xy}}{2}\right)^2 + \left(\frac{\gamma_{xz}}{2}\right)^2 + \left(\frac{\gamma_{yz}}{2}\right)^2\right]} \tag{2}$$

where $\nu_{el} = 0.28$ is the elastic Poisson's ratio, obtained from the measured elastic moduli (E, G) whereas ε_x, ε_y, ε_z, γ_{xy}, γ_{xz} and γ_{yz} are the component of the strain tensor. If one considers that $\varepsilon_x = -\nu_{el}\varepsilon_z$, $\varepsilon_y = -\nu_{el}\varepsilon_z$, and $\gamma_{xy} = \gamma_{yz} \approx 0$, and that due to the axial symmetry of the sample and the applied loadings $\gamma_{yz} = \gamma_{\vartheta z}$, eq. (2) can be rewritten as:

$$\varepsilon_{eq} = \frac{1}{(1+\nu_{el})\sqrt{2}}\sqrt{2(1+\nu_{el})^2{\varepsilon_z}^2 + \frac{3}{2}(\gamma_{\vartheta z})^2} \tag{3}$$

The components of normal and shear strain, in cylindrical coordinates, are calculated as:

$$\varepsilon_z = \frac{u_{z1} - u_{z2}}{L} \tag{4}$$

$$\gamma_{\vartheta z} = \frac{u_{\vartheta 1} - u_{\vartheta 2}}{L} + \frac{1}{R_o}\frac{u_{z1} - u_{z2}}{\Delta\vartheta} \tag{5}$$

Figure 6b shows that results are well fitted by a power law equation $\varepsilon_{eq,a} = a(2N_f)^b$, whose coefficient *a* and exponent *b* are shown in the same figure.

3.2 Failure modes

Different failure modes were observed according to the fatigue resistance, as shown in Figs. 6a and 6b. Typical failure paths are shown in Fig. 6a and schematic representations of the average fracture angles are shown in Fig. 6b. In particular, three failure modes were identified depending on the applied stress amplitude. Fracture surfaces normal to the axis of the sample were observed at the highest values of the applied stress (Type #1 in Table 3, $\sigma_{eq,max}/\sigma_U$=0.61), whereas more complex fracture paths were observed at lower stress amplitudes . In these latter cases it seems that the energy provided by the torsion loading is predominant with respect to the axial one, causing the fracture to grow following a helicoidal path. In fact, crack initiates and early propagates on the maximum shear planes and it approaches the maximum principal stress plane during its propagation.

The different failure modes were also observed on wrought samples under biaxial load condition from experiments carried out respectively by Cryderman et al. [34] and Jensen [35]. Early works by Brown and Miller [36] and of Socie et al. [37,38] give useful insight to understand crack propagation mechanisms under multiaxial loading. In particular, it was shown that cracks nucleate and grow along preferred orientation depending on the material properties and loading conditions. Micro-cracks typically nucleate along the slip systems, that are aligned with the maximum shear plane, in the case of predominant ductile behavior. On the contrary, in mainly brittle materials micro-cracks usually nucleate from discontinuities, such as inclusions or voids, but they can also nucleate along the slip systems aligned with the maximum shear plane. Once micro-cracks nucleate, they grow along maximum shear planes and when they get longer, mode I crack propagation is predominant. Therefore, there is a deviation of the fracture path from the maximum shear plane to the maximum principal stress plane up to the complete failure of the sample.

When dealing with small cracks, normal stress has a secondary influence with respect to the shear. In fact, micro-cracks typically grow with an irregular path according to the slip bands orientation. When crack get longer, normal stress is not negligible anymore because, decreasing the crack closure and friction mechanisms between the crack flanks, it increases the propagation rate.

These observations provided the physical basis for critical plane approaches that reflect the material damage mechanism.

However, the damage evolution associated with different failure modes in AM Ti6Al4V samples are being systematically analyzed, within this research program, by fractographic analyses and *in-situ* micro-tomography investigations [39]. In any case, fracture modes were also observed by the thermographic analysis, that is in terms of crack path evolution during temperature changes during fatigue loading, as shown in Fig. 7. In particular, the figure shows the temperature vs normalized cycles (N/N_f) observed under two different loading conditions: 1) high stress amplitude (Type #1 in Table 3) and 2) low stress amplitude (Type #7 in Table 3). The temperature profile is characterized by three phases: an initial increase of the temperature (phase I), a temperature plateau (phase II) and a rapid increasing when plastic deformations become relevant, that is near to the final fracture (phase III).

As expected, the level of temperature plateau (phase II) is lower for Type #7 loading condition ($\sigma_{eq,max} = 0.28\sigma_U$) and a rapid temperature increase is observed just before the failure (close to the 90% of the fatigue life). Instead, for Type #7 condition ($\sigma_{eq,max} = 0.61\sigma_U$) the higher

temperature plateau is attributed to the higher stresses and deformations and the temperature tends to increase even before the final failure (close to the 75% of the fatigue resistance).

Conclusions

In this study the multiaxial fatigue behavior of thin-walled Ti6Al4V AM specimens, made by the SLM process, under proportional loads was analyzed. Multiaxial conditions were obtained by combining axial and torsional loads. Full field measurement techniques were used to capture temperature and strain evolution during fatigue loading, by infrared thermography (IR) and digital image correlation (DIC). Fatigue curves, in terms of both equivalent stress and strain amplitudes were obtained.

Results revealed different failure modes, depending on the applied stress level. At the first stage of the loading history, the crack nucleates and propagates along the maximum shear plane and it tends to approach the maximum tensile stress direction when it gets longer. Such observations were also confirmed by the analyses of the infrared results. The results provided a first understanding of the multiaxial fatigue behavior of Ti6Al4V AM samples under in-phase loading conditions to compare, in the next future, with the uniaxial and non-proportional multiaxial loads.

References

[1] Inagaki I., Takechi T., Shirai Y., Ariyasu N., 2014. Application and features of titanium for the aerospace industry. Nippon Steel & Sumitomo Metal Technical Report: 22-27.

[2] Boyer R. R., 1996. An overview on the use of titanium in the aerospace industry. Materials Science and Engineering: A: 213 (1):103-114.

[3] Singh P., Pungotra H., Kalsi N. S., 2017. On the characteristics of titanium alloys for the aircraft applications. Materials Today Proceedings: 4 (8):8971-8982.

[4] Uhlmann E., Kersting R., Klein T. B., Cruz M. F., Borille A.V., 2015. Additive manufacturing of titanium alloy for aircraft components. Procedia CIRP: 35:55-60.

[5] Donachie M. J., 2000. Titanium: A Technical Guide, second ed. ASM International, Materials Park, OH.

[6] Cui C., Hu B., Zhao L., Liu S., 2011. Titanium alloy production technology, market prospectsand industry development, Materials: 32 (3):1684-1691.

[7] Huang R., Riddle M., Graziano D., Warren J., Das S., Nimbalkar S., Cresko J., Masanet E., 2016. Energy and emissions saving potential of additive manufacturing: the case of lightweight aircraft components. Journal of Cleaner Production: 135:1559-1570.

[8] ASTM F2792-12a, 2012. Standard Terminology for Additive Manufacturing Technologies (Withdrawn 2015), ASTM International. West Conshohocken, Pennsylvania, PA.

[9] Selcuk C., 2011. Laser metal deposition for powder metallurgy parts, Powder Metallurgy: 54:94-99.

[10] Lewandowski JJ. Seifi M., 2016. Metal additive manufacturing: a review of mechanical properties, Annu Rev Mater Res: 46:14.1-14.36

[11] Froes F., Dutta B., 2014. The additive manufacturing (AM) of titanium alloys, Adv Mater Res: 1019:19-25

[12] Katinas C., Liu S., Shin,Y. C., 2018. Self-sufficient modeling of single track deposition of Ti-6Al-4V with the prediction of capture efficiency. Journal of Manufacturing Science and Engineering: 141 (1) (011001-011001-10).

[13] Liu S., Shin Y. C., 2018. Simulation and experimental studies on microstructure evolution of resolidified dendritic TiCx in laser direct deposited Ti-TiC composite. Materials & Design: 159:212-223

[14] Li P., Warner D., Fatemi A., Phan N., 2016. Critical assessment of the fatigue performance of additively manufactured Ti-6Al-4V and perspective for future research. International Journal of Fatigue 85:130-43.
[15] Tridello A., Fiocchi J., Biffi C. A., Chiandussi G., Rossetto M., Tuissi A., Paolino D. S., 2019. VHCF response of heat-treated SLM Ti6Al4V Gaussian specimens with large loaded volume. Procedia Structural Integrity: 18:314-321.
[16] Wycisk E., Solbach A., Siddique S., Herzog D., Walther F., Emmelmann C., 2014. Effects of defects in laser additive manufactured Ti-6Al-4V on fatigue properties. Physics Procedia 56:371-8.
[17] Fatemi A., Molaei R., Sharifimehr S., Shamsaei N., Phan N., 2017. Multiaxial fatigue behavior of wrought and additive manufactured Ti-6Al-4V including surface finish effect. International Journal of Fatigue 100:347-366.
[18] Edwards P., Ramulu M., 2014. Fatigue performance evaluation of selective laser melted Ti–6Al–4V. Materials Science and Engineering: A: 598:327-37.
[19] Strantza M., Vafadari R., De Baere D., Vrancken B., Van Paepegem W., Vandendael I., Terryn H., Guillaume P., Van Hemelrijck D., 2016. Fatigue of Ti6Al4V structural health monitoring systems produced by selective laser melting. Materials (Basel): 9 (2).
[20] Biswas N., Ding J. L., Balla V. K., Field D. P., Bandyopadhyay, A., 2012. Deformation and fracture behavior of laser processed dense and porous Ti6Al4V alloy under static and dynamic loading, Materials Science and Engineering: A: 549:213-221.
[21] Carroll B. E., Palmer T. A., Beese A. M., 2015. Anisotropic tensile behavior of Ti-6Al-4V components fabricated with directed energy deposition additive manufacturing. Acta Materialia: 87:309-320.
[22] Liu S., Shin Y. C., 2018. Simulation and experimental studies on microstructure evolution of resolidified dendritic TiCx in laser direct deposited Ti-TiC composite. Materials & Design: 159:212-223
[23] Ali H., Ghadbeigi H., Mumtaz K., 2018. Effect of scanning strategies on residual stress and mechanical properties of Selective Laser Melted Ti6Al4V, Materials Science and Engineering: A: 712:175-187.
[24] Wu M. W., Lai P. H., Chen J. K., 2016, Anisotropy in the impact toughness of selective laser melted Ti–6Al–4V alloy. Materials Science and Engineering: A: 650:295-299.
[25] Beretta S., Romano S., 2017. A comparison of fatigue strength sensitivity to defects for materials manufactured by AM or traditional processes, International Journal of Fatigue: 94:178-191.
[26] Leuders S., Thöne M., Riemer A., Niendorf T., Tröster T., Richard H., et al., 2013. On the mechanical behaviour of titanium alloy Ti-6Al-4V manufactured by selective laser melting: fatigue resistance and crack growth performance. Int J Fatigue: 48:300–7.
[27] Fatemi A., Molaei R., Sharifimehr, S., Shamsaei, N., Phan, N., 2017. Torsional fatigue behavior of wrought and additive manufactured Ti-6Al-4V by powder bed fusion including surface finish effect. International Journal of Fatigue: 99:187-201.
[28] Wu Z-R., Hu X-T., Song Y-D., 2014. Multiaxial fatigue life prediction for titanium alloy TC4 under proportional and non-proportional loading. International Journal of Fatigue: 59:170-5.
[29] ASTM E2207–15, 2015. Standard Practice for Strain-Controlled Axial-Torsional Testing with Thin Walled Tube Specimens. ASTM International. West Conshohocken, Pennsylvania, PA.

[30] Stephens R. I., Fatemi A., Stephens R. R., Fuchs H. O., METAL FATIGUE IN ENGINEERING, AWiley-Interscience Publication, Second Edition.
[31] ASTM E1012-14, 2014. Standard Practice for Verification of Testing Frame and Specimen Alignment Under Tensile and Compressive Axial Force Application. ASTM International. West Conshohocken, Pennsylvania, PA.
[32] Socie D. F., Marquis G. B., 2000. Multiaxial fatigue. Society of Automotive Engineers, Inc.
[33] Susmel L., 2009. Multiaxial Notch Fatigue. Taylor & Francis, Inc.
[34] Cryderman R., Shamsaei N., Fatemi A., 2011. Effects of continuous cast section size on torsion deformation and fatigue of 1050 steel shafts. J Mater Process Technol. 211:66–77.
[35] Jensen D. M., 2005. Biaxial fatigue damage behavior of NiTi shape memory alloy. Air Force Institute of Technology, Wright-Patterson Air Force Base, Ohio.
[36] Brown M. W., Miller K. J., 1979. Initiation and groth of cracks in biaxial fatigue. Fatigue Fract. Eng. Mater. Struct. 1:231-246.
[37] Hua C. T., Socie D. F., 1985. Fatigue damage in 1045 steel under variable amplitude biaxial loading. Fatigue Fract. Eng. Mater. Struct. 8:101–14.
[38] Bannantine J. A., Socie D. F., 1988. Observations of cracking behavior in tension and torsion low cycle fatigue. In: Solomon HD, Halford GR, Kaisand LR, Leis BN, editors. ASTM symposium on low cycle fatigue, vol. 942. ASTM STP. p. 899–921.
[39] Renzo D. A., Sgambitterra E., Magarò P., Furgiuele F., Maletta C., Biffi C., Fiocchi J., Tuissi A., 2019. Multiaxial fatigue behavior of additive manufactured Ti-6Al-4V under in-phase stresses. Structural Integrity Procedia,18: 914-920.

Table 1. SLM process parameters used to manufacture the Ti6Al4V samples.

Power	*Exposure time*	*Layer thickness*	*Scanning strategy*	*Spot size*	*Point distance*
400 W	60 μs	60 μm	Meander	65 μm	80 μm

Table 2. Monotonic properties of additive manufactured Ti6Al4V.

Mechanical property	*Axial*				*Shear*			
		AM Measured	AM Fatemi et al. [17]	Wrought Material [17,30]		AM Measured	AM Fatemi et al.-[17]	Wrought material [17]
Elastic modulus [GPa]	E	108.9	109.8	108.2-116	G	42.5	42.5	42
Yield strength [MPa]	σ_Y	798	951	815-944	τ_Y	475	634	523
Ultimate strength [MPa]	σ_U	948	1052	950-1190	τ_U	626	699	-

Table 3. Multiaxial fatigue test conditions (Stress in MPa).

Test type#	*Axial stresses*		*Torsional stresses*		*Equivalent von Mises stresses*			$\sigma_{eq,max}/\sigma_U$
	σ_a	σ_m	τ_a	τ_m	$\sigma_{eq,a}$	$\sigma_{eq,m}$	$\sigma_{eq,max}$	
1	194	215	112	124	275	304	578	0.61
2	175	194	101	112	248	274	521	0.55
3	140	155	81	89	198	219	417	0.44
4	140	155	81	89	198	219	417	0.44
5	124	137	72	79	176	194	370	0.39
6	105	116	61	67	149	164	313	0.33
7	89	99	51	57	126	139	265	0.28
8	64	70	37	41	90	100	190	0.20

Table 4. Multiaxial fatigue test results.

ID sample	$\sigma_{eq,a}$ [MPa]	$\varepsilon_{eq,a}(\%)$	Reversals to failure ($2N_f$)
P1	275	0.268	32318
P2	248	0.242	53148
P3	198	0.193	113182
P4	198	0.188	174632
P5	176	0.164	313260
P6	149	0.138	190012
P7	126	0.118	786726
P8	90	0.088	4000000

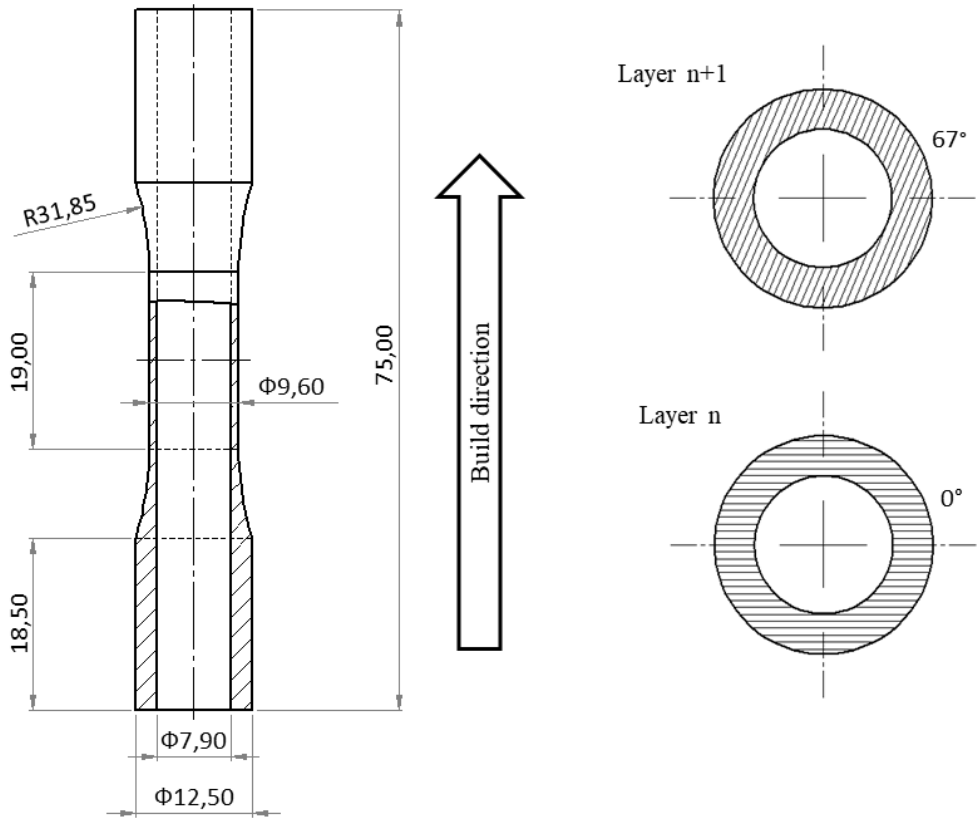

Figure 1 – (a) Thin-walled tubular specimen geometry with nominal dimensions; (b) Laser scanning strategies.

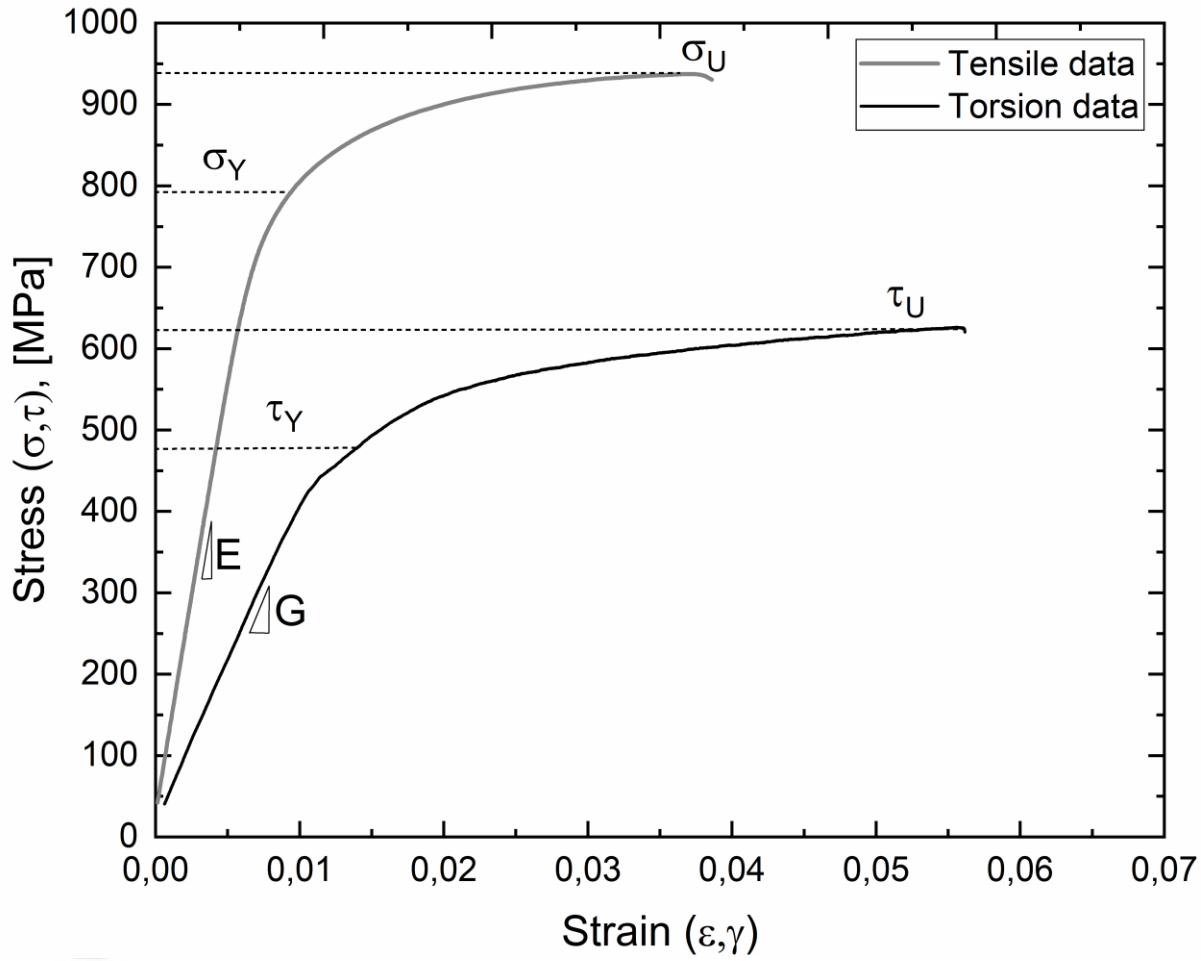

Figure 2 – Monotonic stress-strain and shear stress-shear strain curves of AM specimen.

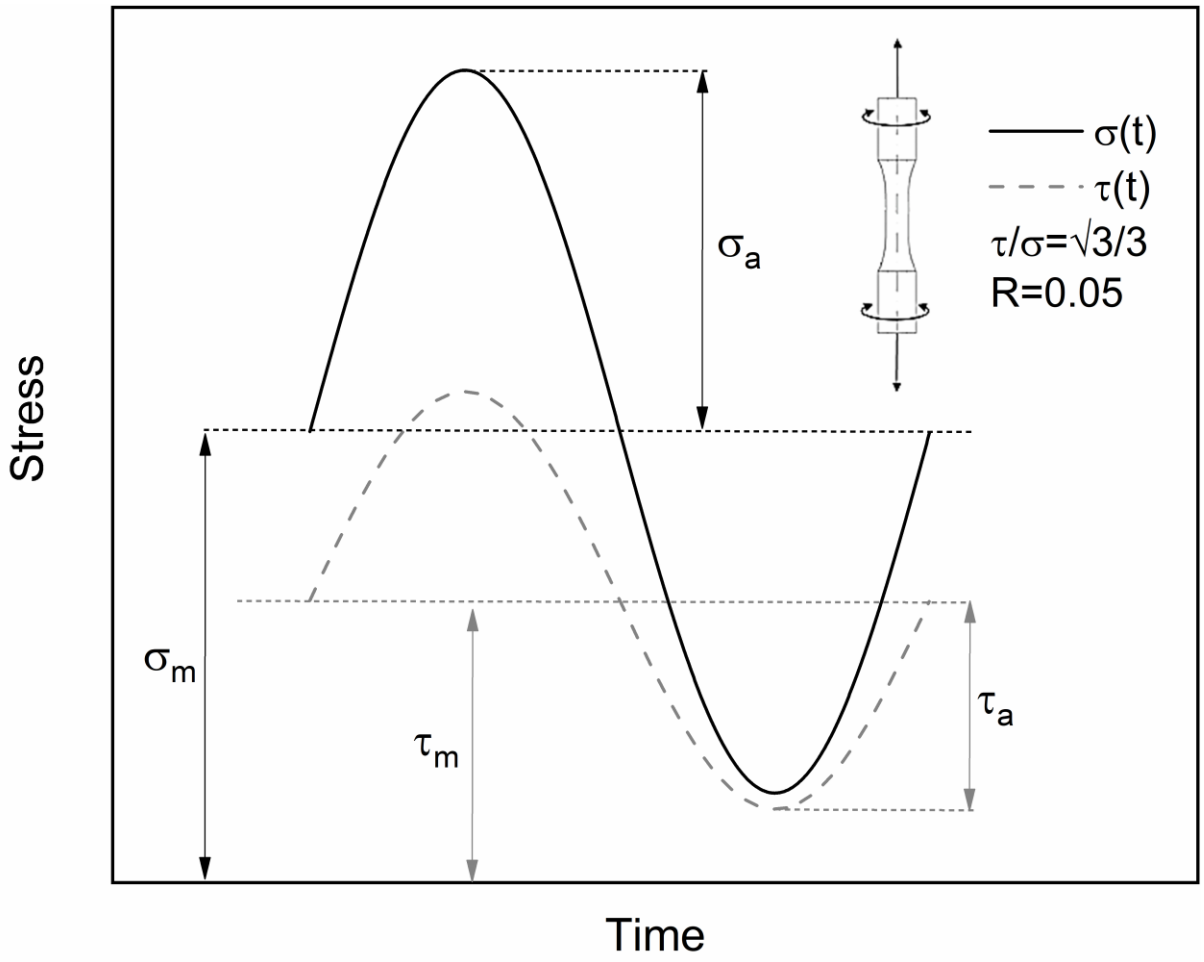

Figure 3 – Schematic depiction of the in-phase axial and torsion stress.

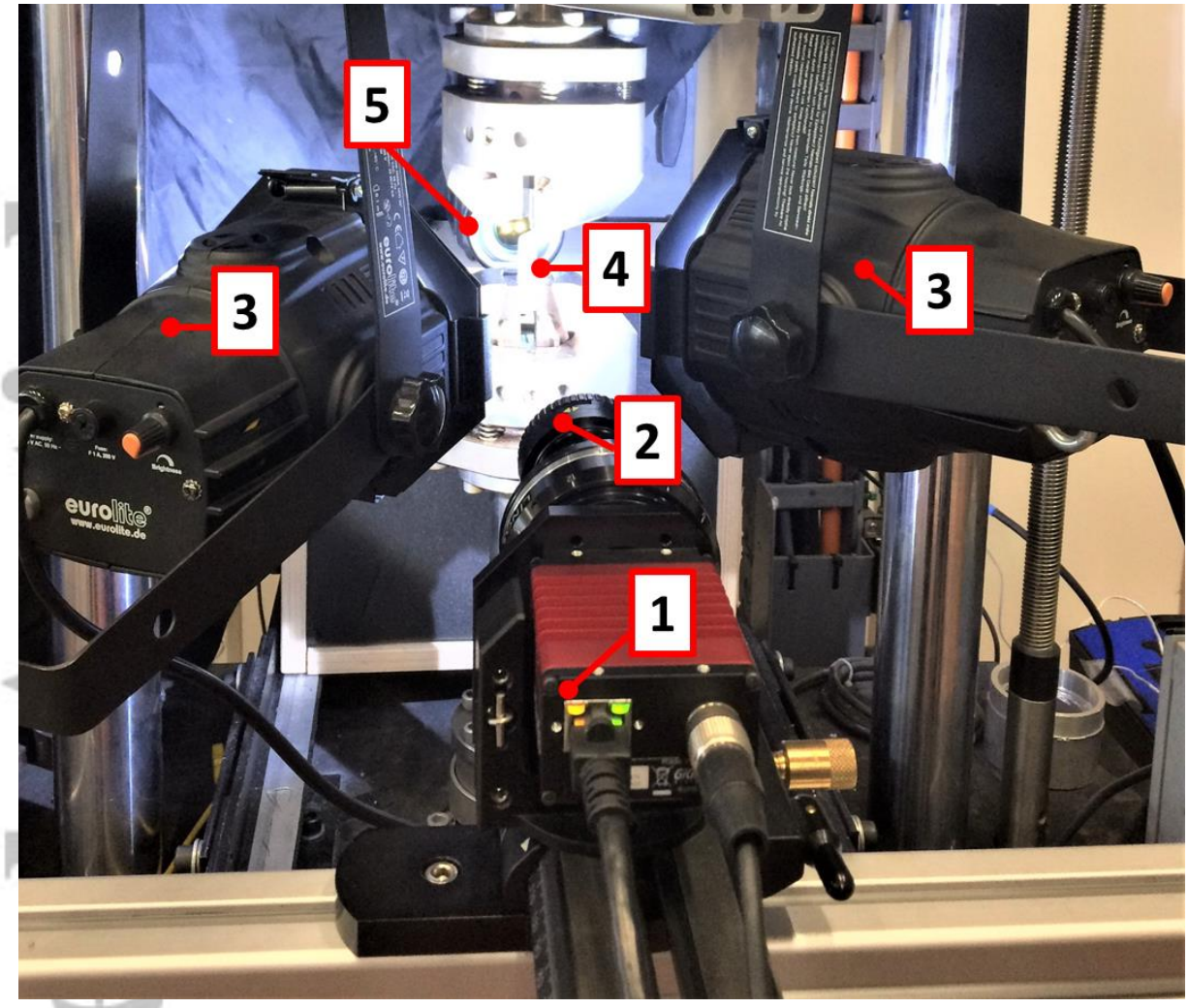

Figure 4 – The experimental setup: (1) digital camera, (2) lens, (3) light source, (4) specimen and (5) infrared-camera.

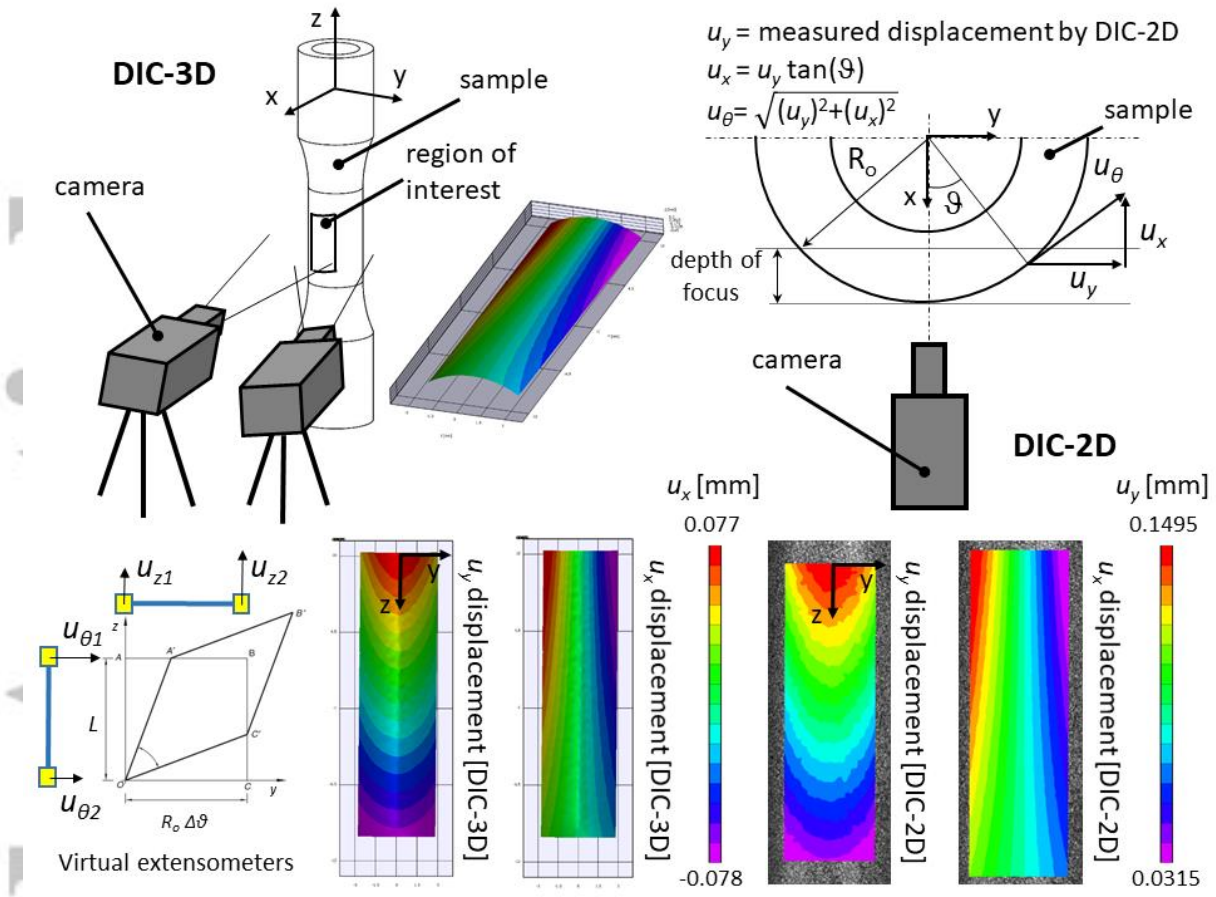

Figure 5 – Comparison between 3D and 2D digital image correlation results and main features for the calculation of the deformations by virtual extensometers.

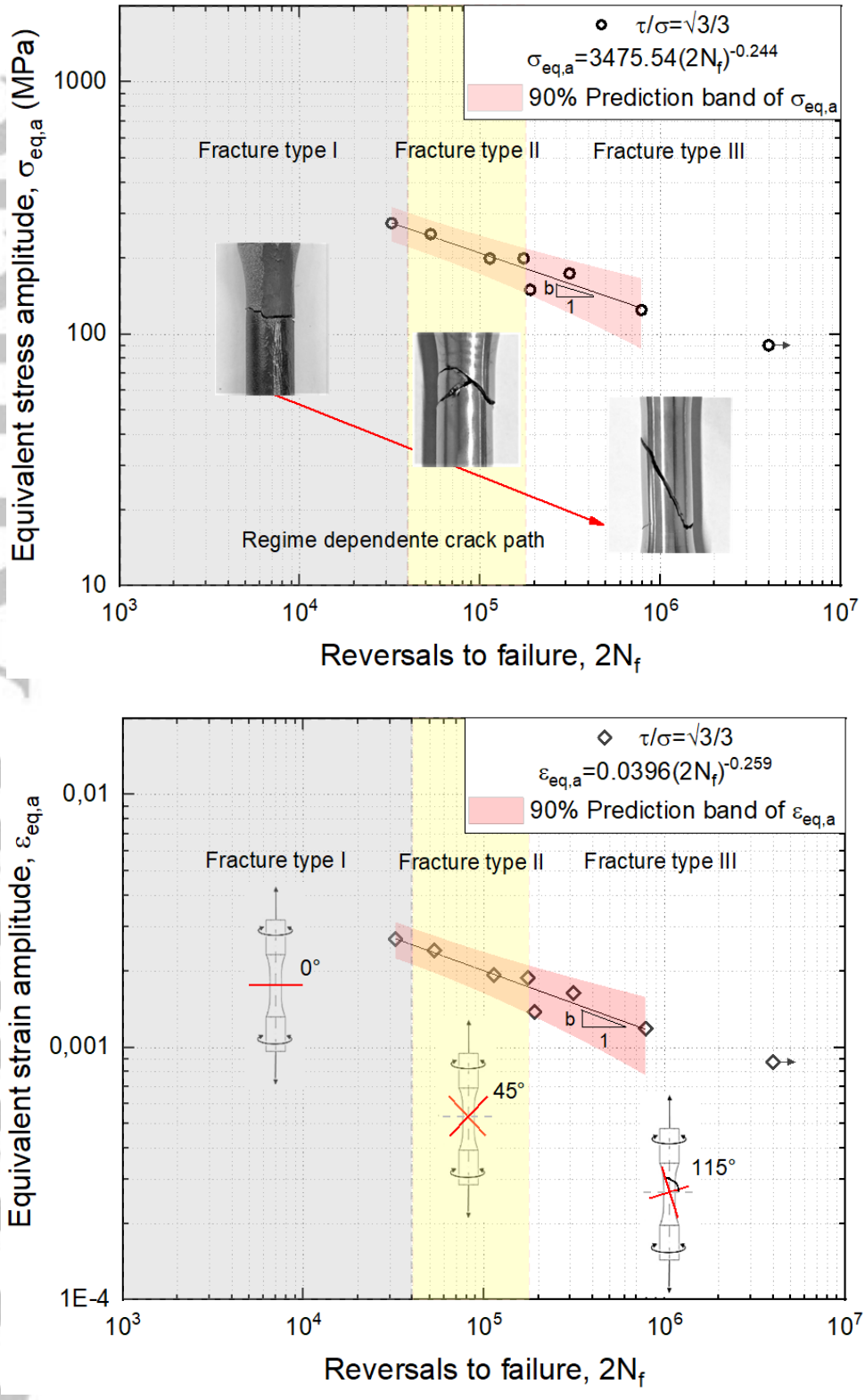

Figure 6 – von Mises equivalent stress amplitude $\sigma_{eq,a}$ (a) and strain amplitude $\varepsilon_{eq,a}$ (b) as a function of the number of reversals to failure ($2N_f$).

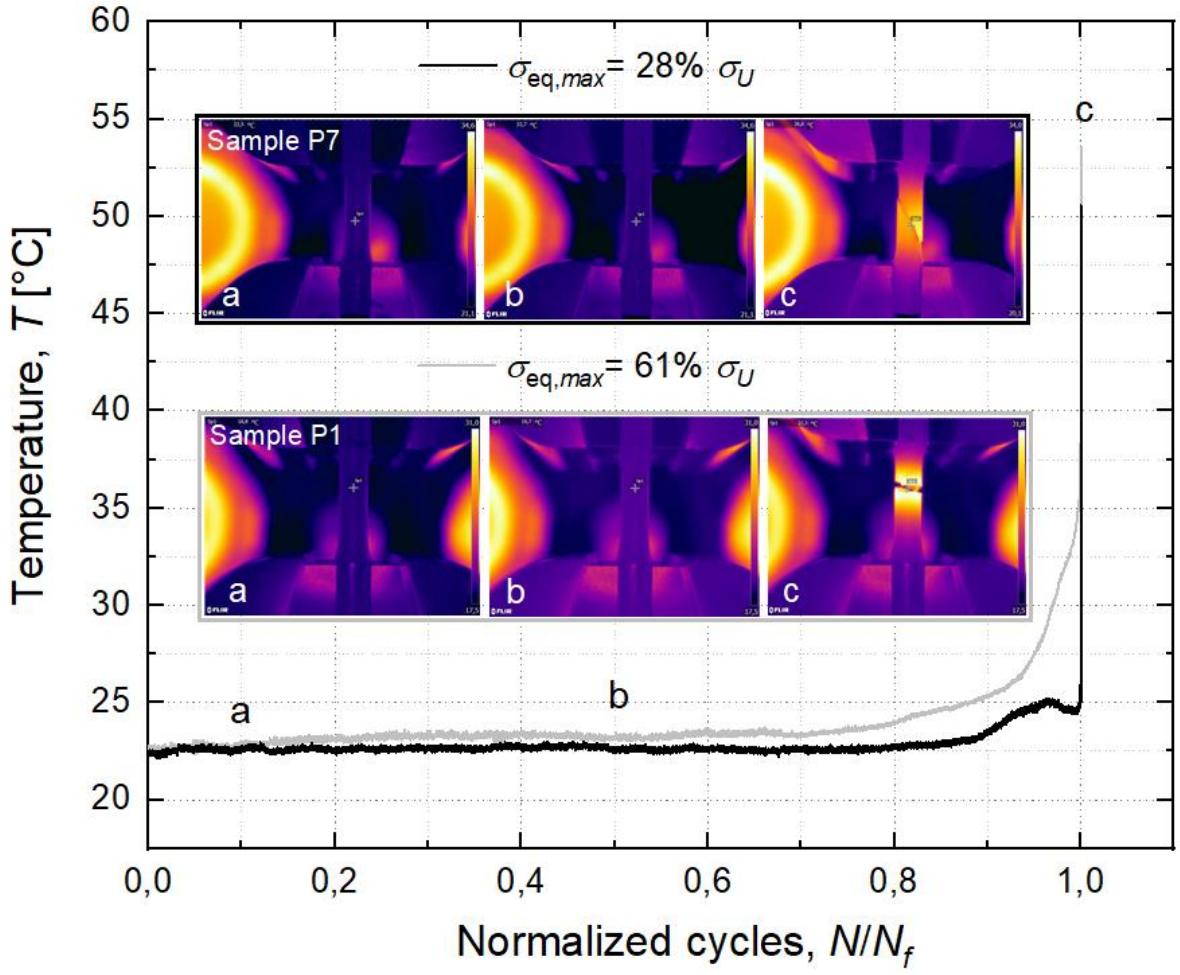

Figure 7 – Temperature trend for two different load conditions.